# Erosion of an Electron-Beam Front in a Long Beam-Plasma System

L. Y. Chan and R. L. Stenzel
*Department of Physics, University of California, Los Angeles, California 90024*
(Received 8 February 1991)

The front of an electron beam ($t_{rise} \approx 20$ ns, $V_b = 200$ V, $I_b \leq 2$ A) injected into a uniform, magnetized plasma ($n_e \approx 2\times10^{11}$ cm$^{-3}$, $kT_e < 0.2$ eV, $B_0 = 90$ G) is observed to erode rapidly because of scattering of the beam electrons via collective beam-plasma interactions. The propagation of the beam front is measured with temporal and axial resolution via beam excitation light. A broadened light front can result that propagates much slower than the injected beam particle speed.

PACS numbers: 52.40.Mj, 52.25.Rv, 52.35.Qz, 52.70.Kz

The study of the propagation of pulsed electron beams into plasmas is important and relevant for many areas of plasma and beam physics, ranging from relativistic electron beams [1,2] to laboratory beam experiments [3] and active beam experiments in the ionosphere [4]. Collective beam-plasma effects can strongly affect the dynamics of even short beams, leading to beam scattering, energetic tail production, and plasma heating. Most laboratory studies on beam-plasma interactions have been performed in steady state [5–7] or on ionic time scales, in which nonlinear effects are explained in terms of ion wave dynamics [3] and density perturbations, such as Langmuir collapse [8]. In contrast, our experiment is time resolved within the front of a propagating electron beam ($t_{rise} < 100 f_{pe}^{-1}$), which is observed to scatter, erode, and broaden rapidly due to noncollisional, collective interactions with the background plasma.

The experimental setup in Fig. 1 consists of a pulsed, glow discharge in a uniform axial magnetic field ($B_0 = 90$ G, $P_{argon} = 4\times10^{-4}$ Torr) and an electron beam (rise time of 20 ns, $V_b = 200$ V, $I_b \leq 2$ A) that is produced by a solid BaO-coated cathode, pulsed rapidly during the afterglow plasma ($n_e = 2\times10^{11}$ cm$^{-3}$, $kT_e < 0.2$ eV). Beam fronts of different currents but similar rise times are injected into a plasma of fixed density by varying the beam heater power only and matching the beam pulser load to 50 Ω with shunt resistors. The beam current is measured with a calibrated current monitor externally and relatively inside the plasma, with a magnetic loop whose signal is integrated; excellent linearity between the two measurements is found. The plasma density and temperature are measured using a Langmuir probe with the beam turned off. When the beam is pulsed on, the plasma parameters should not change significantly during the short propagation time of the beam front. The beam-to-plasma density at injection is then known, since the beam density can be calculated from the beam current, voltage, and diameter. The propagation of the beam front is measured optically with temporal and axial resolution ($\delta t \leq 5$ ns, $\delta z \leq 2$ mm) using a lens-fiber-optics probe that collects light radially across the beam-plasma column and can scan axially along the propagation direction. The light intensity, which is caused by excitation of argon neutrals and ions via collisions with energetic electrons (above ~10 eV), is detected with a photomultiplier tube sensitive in the visible spectrum and measures the total energetic electron particle flux. Single-shot optical signals are spiky due to photon-level detection, but the statistics is improved by averaging over repeated pulses using a digital oscilloscope at a 1-ns/point sampling rate. To avoid boundary effects, only optical features that occur before the beam front reaches the end of the chamber (i.e., $t \leq 100$ ns) are considered in the data presented.

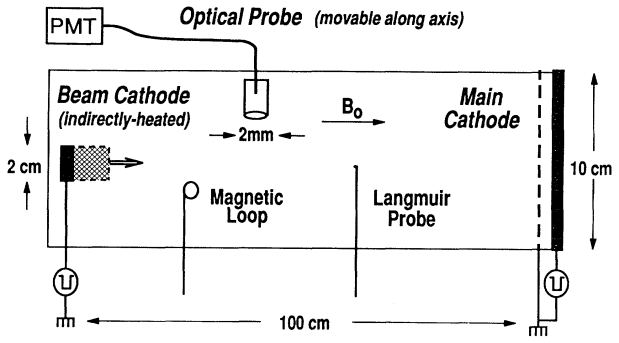


FIG. 1. Schematic diagram of the experimental setup for injecting a sharp electron beam pulse ($t_{rise} \approx 20$ ns, $V_b = 200$ V, $I_b \leq 2$ A) into a uniform, magnetized afterglow plasma ($n_e \approx 2\times10^{11}$ cm$^{-3}$, $kT_e < 0.2$ eV, $B_0 = 90$ G, $P_{argon} = 4\times10^{-4}$ Torr). The propagation of the beam front is measured with temporal and spatial resolution using an optical probe that can scan along the axial direction. The beam current can be varied independently of the beam voltage and plasma density via the cathode heater.

The basic observations are shown in Fig. 2 and may be summarized into three types of beam fronts, depending on beam current. The first type is a linear, noneroding front, in which the optical intensity scales linearly with beam current; this occurs at very low currents where single-particle behavior is expected. The top example (0.3 A) is fairly close to this linear regime, with distinct front and plateau regions, and relatively little change in the front height or slope versus axial distance. The second and third cases (0.6 and 1.3 A) are examples of

 

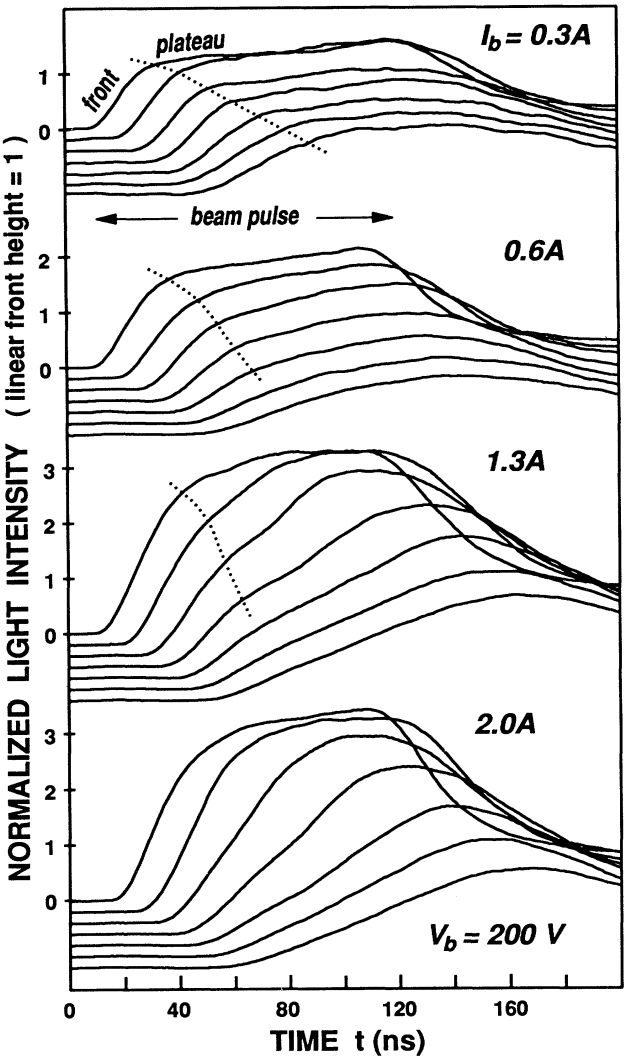


FIG. 2. Three basic types of propagating beam fronts: linearly scaling (0.3 A), eroding (0.6 and 1.3 A), and broadened (2 A). Each is a set of optical signals taken at successive axial distances, from 2.5 to 32.5 cm at intervals of 5 cm, vertically offset for clarity. The top example is very close to single-particle behavior. The dotted lines follow roughly the height of the fronts given by the turning point between each front and its plateau. In the bottom case, the initial front and plateau have merged and are no longer distinguishable. The light intensities are all divided by the beam current and normalized to the front height in the linear regime ($I_b < 0.1$ A, $V_b = 200$ V).

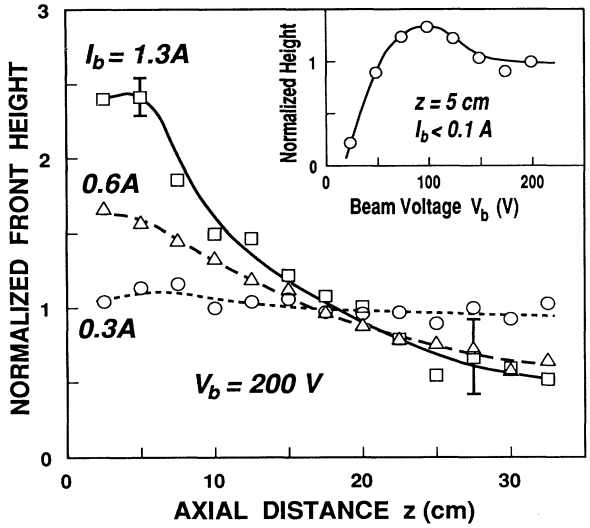


FIG. 3. Axial profiles of the normalized front height for linear and eroding cases. Higher beam currents result in higher nonlinear peak heights and sharper subsequent height decay. The typical uncertainty is small ($< 10\%$ at $z = 5$ cm), but it increases dramatically at positions where the front and plateau slopes converge ($\sim 40\%$ at $z = 27.5$ cm). Inset: The relative optical excitation cross section vs beam voltage, normalized to the value at 200 V.

eroding fronts. Here the front heights, indicated by the dotted lines, decay quickly with axial distance. Note also in the 1.3-A case the merging of the front and plateau regions into a single front as their slopes converge with axial distance. The last type (bottom, 2 A) is a broadened front, where merging has already occurred within 2.5 cm from the cathode to form a wider and higher final front. The distinction between eroding and broadened, however, cannot be based on the beam current only, since the beam rise time and the temporal and axial resolutions of the probe also determine the current at which this transition occurs.

A very important but subtle optical feature is the nonlinear quantitative scaling of the optical intensity versus beam current. For example, doubling the current in the eroding regime can produce a fourfold increase in the optical intensity at the beam front. The analysis for this scaling requires normalizing all optical intensities with respect to the linearly scaling, single-particle regime. Any nonlinearity then points to some collective effect, where we define nonlinearity as any increase in the normalized light above the free-streaming beam electron level. The relative beam excitation cross section versus beam voltage is shown in the inset of Fig. 3 and is obtained directly by measuring the front height in the linear regime ($I_b < 0.1$ A) for different voltages, dividing by beam current, and then normalizing to the value at 200 V. Furthermore, this normalized level is subsequently used as the linear referencing height. In Fig. 2, as the beam current is increased, the normalized heights increase from unity and saturate at about 3 times the linear level. Axially, each normalized front should be injected ($z = 0$ cm) near unity. Unfortunately, this cannot be confirmed directly in the present beam-cathode setup, where closer optical measurements ($z < 2$ cm) cannot be made.

The erosion of the beam front is shown quantitatively

in Fig. 3 in the axial profiles of the front heights. Each height is obtained by least-squares fitting the front and plateau regions with straight lines, solving for the intersection, and then normalizing the height to the linear reference level. Since the front height measures the total energetic electron flux only, the front density cannot be calculated because the initial monoenergetic and paraxial velocity distribution will broaden significantly at the nonlinearly scaling regimes. For the linear case (0.3 A), the normalized heights are close to unity and decay very little. This is consistent with the long electron ionization mean free path ($\sim 2$ m) [9] and elastic-scattering mean free path ($> 1$ m) [10] for our beam voltage and argon pressure. For the eroding regime (0.6 and 1.3 A), each profile peaks much above unity and then decays with axial distance, with higher peak heights and sharper front erosion at higher beam currents. Only the occurrence of scattered beam electrons or energetic tail electrons ($> 50$ eV) can explain these nonlinearly scaling features, which require that the total energetic particle flux or path length increase within the detection volume for the same initial beam flux. A beam electron that has scattered spirals, increasing its path length, even though its energy may remain unchanged. Also the trajectories of scattered and free-streaming beam electrons will overlap axially, increasing the net particle flux. Meanwhile, to conserve beam momentum, the parallel velocity of some beam electrons will be transferred to accelerated background electrons. In summary, the axial erosion of the front is the result of initial scattering of the beam electrons into the perpendicular direction followed by height decay via free-streaming velocity dispersion in the axial direction.

The propagation of the broad front in the nonlinear regimes is determined by the scattered beam electrons and energetic tail electrons. The bulk of the electrons in an eroding front propagate slower than given by the applied beam voltage. This contrast is most obvious in a broadened front, e.g., the half-height point of the merged front (Fig. 2, 2 A) propagates at $\sim 40$ eV compared to the 200-eV injected beam electrons. The onset of the front, however, is least affected by scattering interactions and is found to propagate according to single-particle behavior. By least-squares fitting the base line and front regions, and then solving for the intersection time, the propagation curve for the front onset is obtained for the linear and eroding cases in Fig. 4. The dual slope feature of the curve is simply a single-particle free-streaming effect due to the ramped beam voltage; the fastest electrons are injected later and require finite time to overtake the initial slower ones. The theoretical propagation curve for a voltage ramp at constant current (see Fig. 4, inset) is given by the solid line and gives excellent agreement with the data points. The initial and final velocities were chosen to match the speeds obtained from the data in the initial and final regions (i.e., $V_{\text{init}} = 90 \pm 10$ V and $V_{\text{final}} = 250 \pm 30$ V). The initial speed does not begin at zero, since little

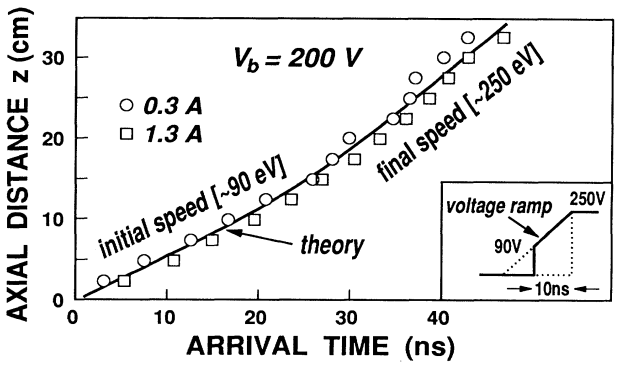


FIG. 4. Propagation curve for the onset of the beam front. The solid curved line is the theoretical solution for single-particle free streaming from the voltage ramp shown in the inset, using the same initial and final speeds found from the data points. The initial speed ($90 \pm 10$ eV) is due to the onset of the optical excitation cross section above 50 V. The final speed ($250 \pm 30$ eV) may indicate some beam acceleration or voltage swings from line mismatch at the beam cathode.

light is produced until the voltage is around 50 V (see Fig. 3, inset). The final speed is higher than expected; this may be due to acceleration of some beam electrons during the scattering process or voltage swings from mismatch in the transmission line at the beam cathode.

High-frequency electrostatic oscillations around the electron plasma frequency have been detected within the beam front using rf antennas, but these results are not included due to length restrictions. Taken together with the strong dependence of the nonlinear optical results on beam current, these measurements point to the beam-generated electron plasma waves as the most plausible source of scattering for the beam electrons. For $I_b = 1.3$ A and $n_e = 2 \times 10^{11}$ cm$^{-3}$, $n_b/n_e$ is 1.5%, and for a rise time of 20 ns or roughly $80 f_{pe}^{-1}$, the gain then exceeds 100 $e$ foldings for the cold beam-plasma instability ($\gamma/\omega_{pe} \approx [n_b/n_e]^{1/3} \approx 0.25$) [11]. Therefore, there is enough time for Langmuir waves to grow from noise to large amplitudes within the beam front. In addition to scattering from plasma waves, time-varying space-charge fields from an unneutralized beam front could also lead to beam scattering. On the other hand, ions do not undergo a single oscillation during the beam front ($\omega_{pi} \Delta t < 1$); therefore Langmuir collapse [8,12,13] and parametric instabilities involving ion waves [3,14] can be discounted. Ionization effects via a beam-plasma discharge are insignificant on the time scale of the beam front [15]. Finally, an important lesson of the experiment is that while a broadened front appears like a noneroding beam front, except for the slower rise time and propagation speed, it should not be mistaken for a linear front, nor should its propagation be misinterpreted via single-particle motions.

In conclusion, we have observed a rapid erosion of the front of a cold electron beam, which can be understood in

terms of scattering of the injected beam electrons from nonlinear interactions with the background magnetized plasma. This mechanism can also lead to the formation of a broad, slowly propagating particle front. These results are important for the propagation of rapidly pulsed, moderately dense ($n_b/n_e < 1\%$) electron beams into plasmas and also demonstrate that the generation of energetic electron tails is not always indicative of Langmuir wave collapse.

This work was supported in part by the Grants No. NSF PHY 87-13929, No. ATM 90-12709, and No. NASA NAGW-1570.

[1] W. W. Destler, P. G. O'Shea, and M. Reiser, Phys. Fluids **27**, 1897 (1984).
[2] J. B. Rosenzweig *et al.*, Phys. Rev. Lett. **61**, 98 (1988).
[3] D. A. Whelan and R. L. Stenzel, Phys. Fluids **28**, 958 (1985).
[4] J. R. Winckler, Rev. Geophys. Space Phys. **18**, 659 (1980).
[5] J. R. Apel, Phys. Fluids **12**, 291 (1969); **12**, 640 (1969).
[6] J. H. Malmberg and C. B. Wharton, Phys. Fluids **12**, 2600 (1969).
[7] W. Carr, J. Ryan, and M. Seidl, Phys. Fluids **24**, 926 (1981).
[8] P. Y. Cheung and A. Y. Wong, Phys. Fluids **28**, 1538 (1985).
[9] D. Rapp and P. Englander-Golden, J. Chem. Phys. **43**, 1464 (1965).
[10] R. Brode, Rev. Mod. Phys. **5**, 257 (1933).
[11] S. Kainer, J. Dawson, R. Shanny, and T. Coffey, Phys. Fluids **15**, 493 (1972).
[12] P. A. Robinson and D. L. Newman, Phys. Fluids B **2**, 3120 (1990).
[13] M. V. Goldman, G. F. Reiter, and D. R. Nicholson, Phys. Fluids **23**, 388 (1980).
[14] S. Bardwell and M. V. Goldman, Astrophys. J. **209**, 912 (1976).
[15] K. Papadopoulus, Comments Plasma Phys. Controlled Fusion **9**, 11 (1984).